

A Novel Robotic Surveying Technique for  
Free-Falling Penetrometers

by

Samuel Ifeoluwa Akinwande

A Thesis Submitted to the the Faculty of the  
Department of Mechanical Engineering  
Cullen College of Engineering

in partial fulfillment of the requirements for the degree of  
Bachelor of Science  
in Mechanical Engineering

Chair of Committee: Dr. Ralph Metcalfe

Co-Chair of Committee: Dr. Aaron T. Becker

Committe Member: Dr. Fritz Claydon

University of Houston

May 2020

© Copyright 2020, Samuel Ifeoluwa Akinwande

## Acknowledgements

First and foremost I thank Victor Montano and Ami Shah for their hard work and support in completing this project. This project could not have been completed without Victor's leadership and Ami's dedication.

I also thank Dr. Aaron Becker for his mentorship and support of my interest in robotics. I am grateful for the opportunity to complete my thesis under his guidance. By encouraging me to explore robotics projects as a freshman, he laid the foundation for this thesis and for my future career in robotics.

Let me express my gratitude to Dr. Jerrod Henderson from the Program for the Mastery of Engineering Studies (PROMES) for his active support of my development as a student and a researcher. I am also grateful to Dr. Jane Grande-Allen from the Bioscience Research Collaborative (BRC) at Rice University for her early encouragement of my interests as a budding researcher.

Finally, I thank my family for supporting me as an engineering student and an undergraduate researcher. I could not have managed the workload without their help and encouragement.

# Abstract

Severe floods and sea level rise (SLR) are increasingly urgent effects of global climate change. Wetlands are natural buffers that prevent inundation and destruction from floods. Anthropogenic destruction of wetlands is reducing their effectiveness as flood buffers. Rapid and timely assessment methods are needed for the effective restoration of the wetlands. This thesis presents a novel method for performing free falling penetrometer (FFP) tests for soft wetland soils. The method involves the aerial deployment of a custom FFP using a consumer quadcopter. The method was tested in three soils to examine the effect of drop height on the FFP deceleration profile and penetration depth. Further tests were conducted to determine the force required to extract the FFP after a successful drop. The effects of speed and angle on extraction force was analyzed. Field tests were simulated by conducting limited indoor surveys with the FFP and a consumer drone. The custom FFP was successful in distinguishing wetland soils in drop experiments. The relationships between drop height, penetration depth and deceleration profile were characterized. Data from extraction tests revealed a linear relationship between extraction force and speed; and an inverse relationship between extraction force and angle. By utilizing techniques to minimize the extraction force, a consumer drone was successful in deploying and retrieving the custom FFP. Further field tests are needed to validate the robustness of the novel method. If proven reliable, this method will be useful in reducing the financial and labor costs associated with wetlands surveys.

# Table of Contents

<b>Acknowledgements</b>	<b>iii</b>
<b>Abstract</b>	<b>iv</b>
<b>Table of Contents</b>	<b>v</b>
<b>List of Figures</b>	<b>vi</b>
<b>Nomenclature</b>	<b>x</b>
<b>1 Introduction</b>	<b>1</b>
1.1 Motivation . . . . .	1
1.2 Existing Methods . . . . .	2
1.3 Proposed Work . . . . .	5
1.4 Contributions . . . . .	6
<b>2 Related Work</b>	<b>8</b>
2.1 Cone Penetrometers . . . . .	8
2.2 Existing Free-Falling Penetrometers . . . . .	9
2.3 UAV Sensor Deployment . . . . .	10

2.4	UAV/Slung Load Dynamics . . . . .	12
<b>3</b>	<b>Methodology</b>	<b>16</b>
3.1	Custom Free-Falling Penetrometer . . . . .	16
3.2	The Deployment Vehicle . . . . .	17
3.3	Description of Soils . . . . .	18
3.4	Test Beds . . . . .	19
3.4.1	Drop Test Bed . . . . .	19
3.4.2	Linear Actuator Extraction Test Bed . . . . .	20
3.4.3	Drone Dynamics and Stability Test Bed . . . . .	21
3.4.4	Quadcopter Deployment Test Bed . . . . .	24
3.4.5	Reel Mechanism Test Bed . . . . .	26
<b>4</b>	<b>Results and Discussion</b>	<b>28</b>
4.1	Drop Tests . . . . .	28
4.2	Actuator Extraction Tests . . . . .	31
4.3	Quadcopter Dynamics and Stability Tests . . . . .	32
4.4	Deployment Tests . . . . .	35
4.4.1	Reel Mechanism Tests . . . . .	37
<b>5</b>	<b>Conclusion</b>	<b>38</b>
5.1	Future Work . . . . .	39
	<b>References</b>	<b>40</b>

## List of Figures

1.1	Regions experiencing wetlands loss, reprinted from the Status and Trends of Wetlands in the Conterminous United States 2004 to 2009 (US Fish and Wildlife Service, 2011) [5] . . . . .	2
1.2	Logistics of a core collection expedition, reprinted from New Jersey (USA) Wetlands Past, Present and Future: Using Sediment Archives to Inform and Guide Wetland Protection, Restoration and Resilience (New Jersey Department of Environmental Protection) [14] . . . . .	3
1.3	Standard coring device, reprinted from the Standard Operating Procedure for Collection of Sediment Samples: GSL Impounded Wetland 2012 Monitoring Activities (Utah Department of Environmental Quality) [2] . . . . .	4
1.4	Overview of proposed wetlands surveying method; typical wetlands environment (left), ecologically invasive conventional sampling expedition (middle), minimally invasive proposed sampling expedition (right) . . . . .	6
2.1	Traditional CPT expedition . . . . .	9
2.2	UAV deployment of SeismicDart and SeismicSpider, reprinted from A Heterogeneous Robotics Team for Large-Scale Seismic Sensing (IEEE Robotics and Automation Letters, 2017) [18]. . . . .	11

2.3	Free body diagram of a generic quadcopter, reprinted from Adaptive Controller Design for Generic Quadrotor Aircraft Platform Subject to Slung Load (IEEE 28th Canadian Conference on Electrical and Computer Engineering, 2015) [6]. . . . .	13
2.4	Generic quadcopter with an attached load, reprinted from Adaptive Controller Design for Generic Quadrotor Aircraft Platform Subject to Slung Load (IEEE 28th Canadian Conference on Electrical and Computer Engineering, 2015) [6]. . . . .	15
3.1	Custom FFP design with embedded electronics . . . . .	17
3.2	FFP deployment vehicle, shown in loaded and unloaded configurations	18
3.3	Representative specimen of wetlands soil used in this experiment. . .	19
3.4	Drop test-bed with pulley. . . . .	20
3.5	Schematic of the linear actuator test-bed showing vertical and angled tests. . . . .	21
3.6	The drone dynamics and stability test platform early model (left) and final model (right). . . . .	22
3.7	Detailed view of the bearing block/counterweight/load cell assembly.	23
3.8	FFP deployment using a UAV. . . . .	24
3.9	Schematics of sacrificial sleeve tests . . . . .	25
3.10	Successful extraction of FFP . . . . .	26
3.11	Reel mechanism (incomplete) . . . . .	27
4.1	Measuring the effect of a 1.5m drop on FFP acceleration-time history	29
4.2	Height: 2.5 m . . . . .	29

4.3	Height: 3.7 m . . . . .	30
4.4	Penetration Depth as a function of drop height and soil type. . . . .	31
4.5	Relationship between extraction force and extraction angle . . . . .	32
4.6	Relationship between extraction force and extraction speed . . . . .	33
4.7	Maximum drone lift at 90° . . . . .	34
4.8	Angular drone lifting forces . . . . .	34
4.9	FFP extraction attempts, blue: extraction without a sacrificial sleeve, red: extraction with a sacrificial sleeve . . . . .	36

# Nomenclature

**SLR:** Sea Level Rise

**FFP:** Free Falling Penetrometer

**CPT:** Cone Penetrometer Test

**UAV:** Unmanned Aerial Vehicle

**UH:** University of Houston

**COTS:** Commercial Off The Shelf

**Li-Po:** Lithium - Potassium

**P/N:** Part Number

**GTOW:** Gross Take Off Weight

# Chapter 1

## Introduction

### 1.1 Motivation

The effects of global climate change are gradually becoming apparent in various regions of the globe. Accelerating sea level rise (SLR) is one of the numerous effects of global climate change. While the impacts of sea level rise will be felt globally, coastal communities are especially at risk. Immediate impacts on coastal communities include severe coastal storms, storm surge floods, and coastal erosion [13].

More than 50% of the U.S. population lives within coastal communities and this number is expected to rise with states like Texas and Florida accounting for the majority of the increase. Unfortunately, these states are also experiencing higher-than-average rates of SLR. Sections of the Texas and Louisiana coastlines experience SLR at rates 2 to 3 times the national average [13].

Wetlands serve as natural buffers against environmental stressors caused by SLR. If properly maintained, wetlands can develop into swamps and marshes that prevent floodwaters from inundating coastal communities. Unfortunately, accelerated SLR and other anthropogenic factors are gradually destroying wetlands. The dangers resulting from the continued loss of wetlands cannot be overstated. Potential impacts include more destructive floods, widespread inundation, coastline erosion, and the abandonment of coastal communities. In the continental United States, many coastal

regions experiencing population increase are also experiencing disproportionate rates of wetlands loss [5]. Regions experiencing disproportionate rates of wetlands loss are shown in Fig. 1.1.

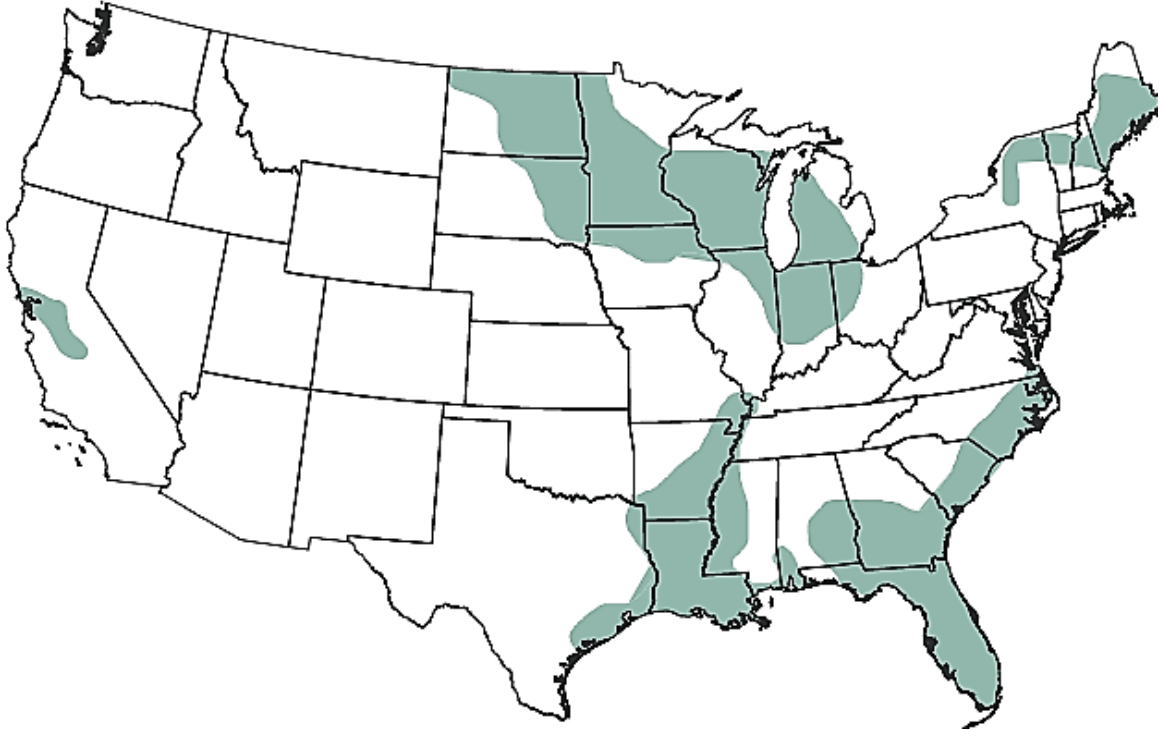


Figure 1.1: Regions experiencing wetlands loss, reprinted from the Status and Trends of Wetlands in the Conterminous United States 2004 to 2009 (US Fish and Wildlife Service, 2011) [5]

Effective protection and restoration of the wetlands requires timely and accurate information about the state of the wetlands. To respond to the various threats facing the wetlands, scientists need safe and reliable methods of assessing the rapidly changing properties of the wetlands.

## 1.2 Existing Methods

Existing methods for assessing vulnerable wetlands typically involve landscape-scale assessment, biological/physiochemical measurements, and rapid assessment protocols. These methods require the collection and processing of soil core samples [7].

After collection, the core samples are usually transported to a centralized location to be dried in a furnace. The processed cores are used to estimate the biological and physical properties of the wetlands. These properties are indicative of the health and resilience of the the wetland ecosystem

Core collection in the wetlands often involves significant labor and capital expenditure. Common expenses include measuring equipment, labor costs, transportation costs, and safety equipment. The general process for a core collection expedition is shown in Fig. 1.2.

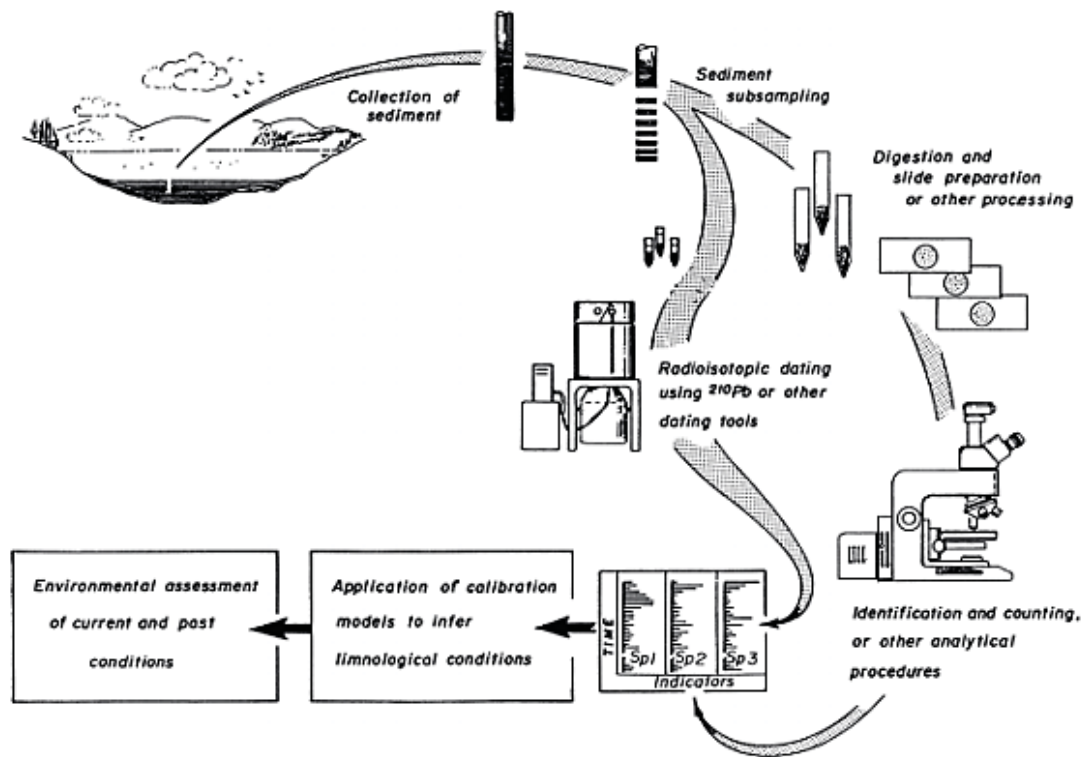


Figure 1.2: Logistics of a core collection expedition, reprinted from New Jersey (USA) Wetlands Past, Present and Future: Using Sediment Archives to Inform and Guide Wetland Protection, Restoration and Resilience (New Jersey Department of Environmental Protection) [14] .

Samples are usually collected using commercially available coring devices. A standard coring device is shown in Fig. 1.3. These devices allow scientists to collect

multiple sedimentary core specimens for further analysis.

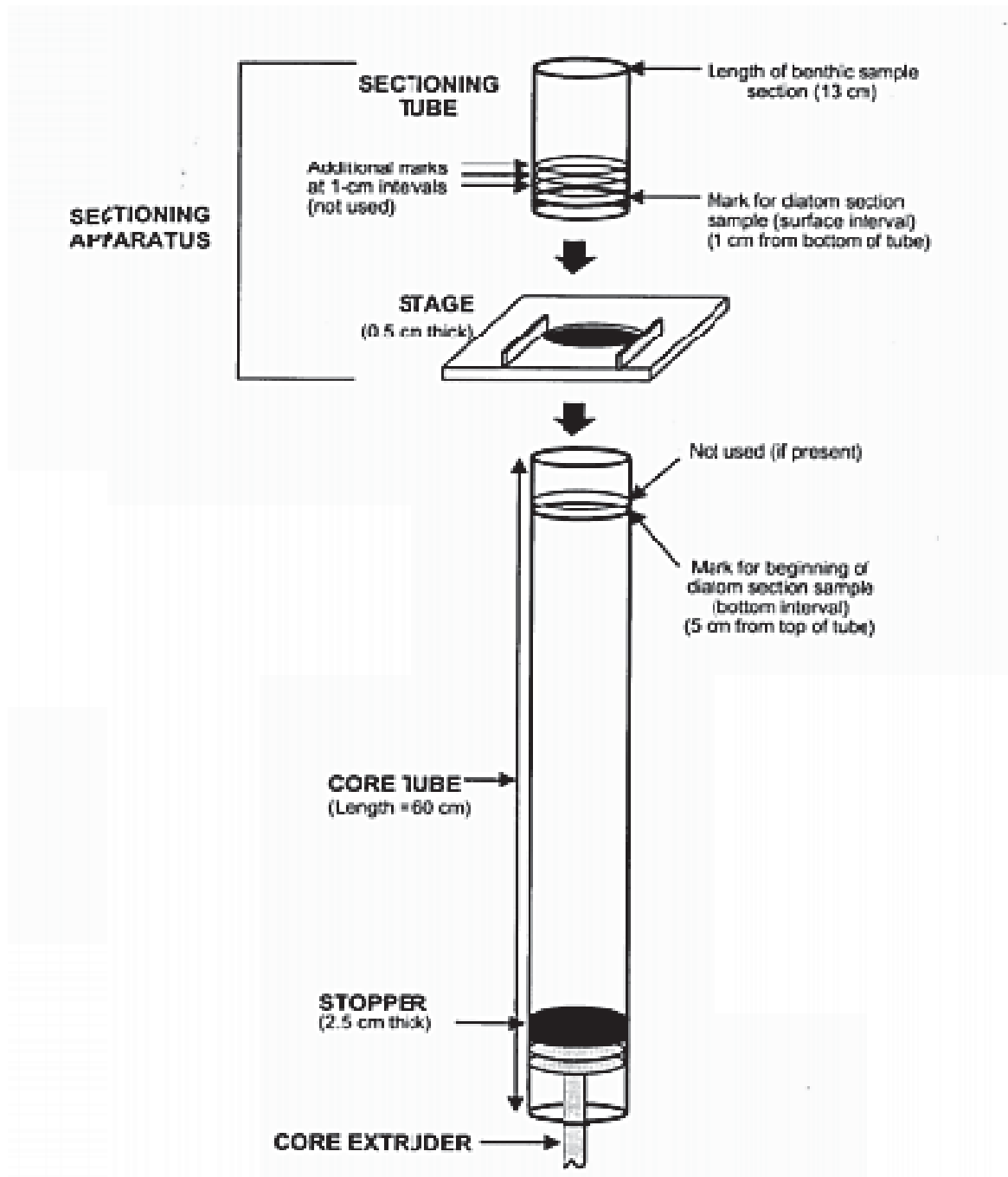


Figure 1.3: Standard coring device, reprinted from the Standard Operating Procedure for Collection of Sediment Samples: GSL Impounded Wetland 2012 Monitoring Activities (Utah Department of Environmental Quality) [2]

A full expedition typically requires mobilizing scientists and expensive equip-

ment into the wetlands. The disturbance to the wetland ecosystem caused by this mobilization increases the risk of accidental contact with wildlife. Creatures commonly found in the wetlands include alligators and multiple species of venomous snakes. Potential contact with some of these creatures makes assessing wetlands a risky endeavor.

Besides the enormous labor and financial risk involved in wetlands core collection expeditions, the data recorded are often unreliable. Errors can be introduced during collection and processing. Common errors include measurement errors due to inconsistent operational procedure, variation in the physical dimensions of coring devices, sediment compression during the coring and/or extraction process, imprecise sectioning of the core into known volumes, variation in the drying and/or furnace temperatures, and the presence of precipitated salts in the sample [7].

### **1.3 Proposed Work**

Errors associated with core collection and processing can be avoided by introducing a custom-designed free-falling penetrometer (FFP) designed by engineers at the University of Houston (UH). The UH FFP was designed to be released from heights ranging from two (2) to five (5) meters. Soil properties can be obtained from acceleration-time history data recorded by sensors in the FFP. By avoiding the need for core sample collection, the labor and financial cost of wetlands surveys can be reduced.

This thesis is part of an initiative to develop rapid assessment protocols and provide new knowledge to enhance the fundamental principles underpinning wetlands assessment models. The thesis is meant to offer insight into the procedure for quadcopter-assisted soil classification. Remote testing will enable scientists to collect wetlands data without incurring the costs associated with traditional techniques.

A data collection expedition using the proposed method will minimize the ecological disturbance prevalent in conventional sampling expeditions. The proposed method is compared to existing sampling expeditions in Fig. 1.4.



Figure 1.4: Overview of proposed wetlands surveying method; typical wetlands environment (left), ecologically invasive conventional sampling expedition (middle), minimally invasive proposed sampling expedition (right)

The costs associated with a typical expedition can be reduced by eliminating the need to store and transport samples. An expedition using the proposed method will require multiple FFPs, consumer quadcopters, and other standard accessories. The quadcopter(s) will be deployed from a convenient central location (like a boat) as shown in Fig. 1.4. Upon arriving at a specified GPS coordinate, the quadcopter will release the FFP and store deceleration data. The process is repeated at each GPS coordinate and the deceleration data is used to categorize soil types.

Subsequent chapters explore prior research on free-falling penetrometers and quadcopter surveying techniques. The validation process for the proposed surveying technique is provided in Chapter 3. The data and results are presented in Chapter 4 and the conclusions are presented in Chapter 5.

## 1.4 Contributions

The scope of this thesis project does not include the design of the FFP. The robot, sensors, and test-beds were designed as part of a team project. My contri-

butions include the design, fabrication, and testing of the extraction test-bed, the dynamics and stability test bed, the deployment test-bed, and the reel mechanism test-bed. The FFP and its electrical system were designed, built, and tested by Victor Montano and Ami Shah. Details about the novel deployment method are presented in a conference paper [3].

## Chapter 2

### Related Work

This chapter describes the current methods for soil classification. These methods include cone penetrometer tests (CPT) and free-falling penetrometers. Existing research on aerially deployed sensors and quadcopter dynamics are also presented.

#### 2.1 Cone Penetrometers

Cone penetrometers are often used in evaluating the material properties, geotechnical units and subsurface stratigraphy for the design of civil infrastructure [4]. The standard cone penetrometer consists of a  $1m$  long,  $0.1m$  diameter cone with a  $60^\circ$  tip. This tip is inserted into soil samples at a rate of  $20mm/s$ . As the cone penetrates the soil, the tip and sleeve resistance, along with pore-water pressure are measured. The combination of tip resistance, sleeve resistance, and pore pressure are used to identify various soil types and estimate properties like shear strength, stress history, and stiffness. Data from cone penetrometer tests (CPTs) inform the design of building foundations, bridges, levees, dams and other infrastructure. CPT data is also used to estimate the probability of liquefaction of sands and tailings dams during earthquakes. Recent uses of the CPT involve applying the test in coastal and offshore environments. Unfortunately, coastal tests involving the CPT are often expensive and labor intensive. A standard CPT expedition is shown in Fig. 2.1.

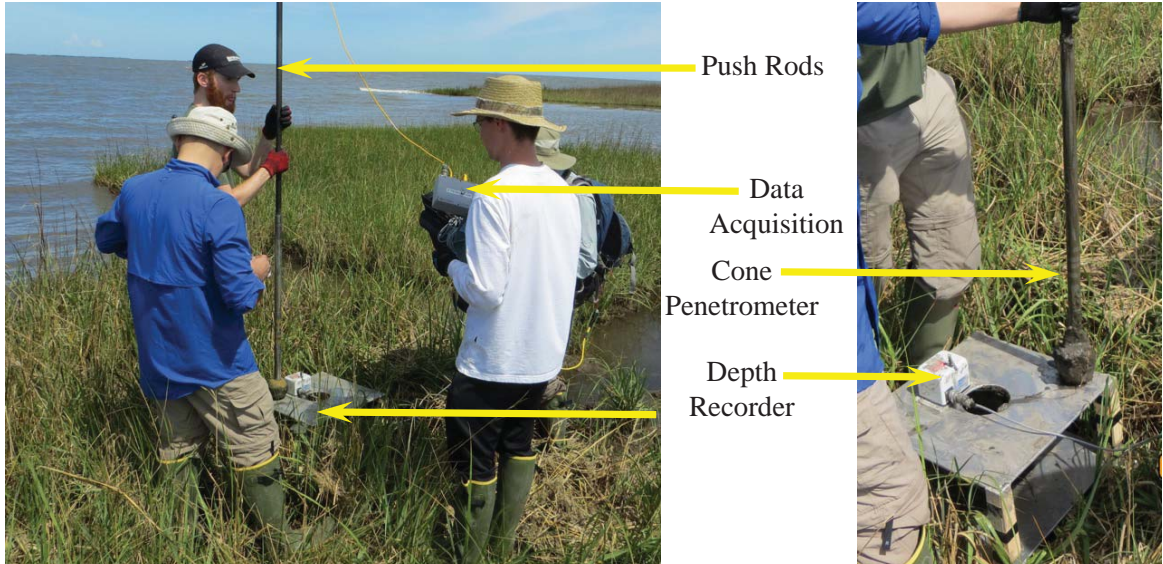


Figure 2.1: Traditional CPT expedition

## 2.2 Existing Free-Falling Penetrometers

Free-Falling Penetrometers (FFPs) were developed to address the limitations of conventional CPTs. In particular, FFPs were developed to explore and identify sediments on the seabed. Researchers in [8] dropped a custom-designed FFP into the ocean to accelerate to a terminal velocity. The deceleration of the FFP was captured by a series of accelerometers embedded in the FFP. The acceleration-time history of the FFP was characterized by the equation

$$v(t) = v_o + \int_0^t a(t)dt, \quad (2.1)$$

where  $v_o$  is the release velocity of the FFP at  $t = 0$  and  $a(t)$  is the acceleration-time history of the FFP recorded by the accelerometers. The data from these tests are used to determine firmness, embedment depth, and mean grain size of the soil sample. The acceleration-time history is also used to estimate the quasi-static bearing capacity of the sediment.

Other innovative applications of FFP data include analyzing the dynamics of clay samples [11], characterizing soil types by correlating pore pressures from high-

velocity FFP impacts [10, 9], measuring static resistance in sand [21], and measuring arctic coastal zones [15].

The FFP developed by the UH Robotic Swarm Control lab builds on existing FFP concepts. However, existing FFPs are designed to penetrate subsea soils. The rapid assessment method described in this thesis requires aerial deployment of the FFP. Subaerial soils are often more complex than submarine soils because offshore deposits are loose and soft. Terrestrial soils often include roots and vegetation and thus, vary significantly in sample size and stiffness. These complexities make the penetration of subaerial soils difficult. The penetration depth of an FFP is a function of its impact velocity while the impact velocity is a function of the FFP's drop height. Vertical penetration at a high velocity is necessary to improve the FFP's ability to penetrate subaerial soils.

## 2.3 UAV Sensor Deployment

Given the recent ubiquity of cheap, commercial off-the shelf (COTS) UAVs, many researchers are actively exploring the feasibility of UAVs for remote sensing. Researchers in [20] designed an auger for remote sensor installation while researchers in [12] created a method to validate sensor deployment.

Prior research projects in the UH Robotic Swarm Control Lab have explored the role of UAVs in deploying different geological sensors [16, 17, 18]. The logistics of drone deployment of geophone sensors were explored in [16, 17].

The drone-deployed geophones were used to measure geological vibrations and the results were comparable to conventionally deployed geophones. The challenges encountered in the geophone deployment experiments can be extrapolated to FFP deployment experiments. Of particular interest is the relationship between release height, penetration depth, and deviation angle. These factors are critical in obtaining



Figure 2.2: UAV deployment of SeismicDart and SeismicSpider, reprinted from A Heterogeneous Robotics Team for Large-Scale Seismic Sensing (IEEE Robotics and Automation Letters, 2017) [18].

accurate vibration data from the geophones. The nature of the deployment vehicle introduced inconsistencies in the recorded data. In [18], a geophonic equivalent of a free-falling penetrometer (FFP) is introduced. The sensor was dubbed the SeismicDart and a UAV is equipped with a mechanism to deploy up to four (4) darts. The dart and its deployment vehicle are shown in Fig. 2.2. The dart deployment method is similar to the proposed deployment method for the custom-designed FFP. The UAV is equipped with an autopilot computer (a PixHawk) and it is able to deploy the darts autonomously. It is interesting to note that the SeismicDart retrieval

process requires manual intervention. The paper also introduces a ground robot to assist in data collection. A common theme among existing UAV surveying projects is the challenge of autonomously retrieving sensors deployed by UAVs. This thesis introduces a customizable mechanism for the autonomous deployment and retrieval of sensors using UAVs.

## 2.4 UAV/Slung Load Dynamics

Mounting a sensor onto a quadcopter introduces instability to the system. The free-falling penetrometer (FFP) will be mounted onto a commercial quadcopter using a rigid cord. While deployed, the FFP may exhibit pendulous behavior relative to the UAV. There exists a need to characterize the behavior of the quadcopter/FFP system. The pendulous behavior of the FFP may be modeled as a slung load attached to a quadcopter. Researchers in [6] created an applicable model of a generic quadcopter/slung load system. The following section replicates the model created in [6]. The free-body diagram of the generic quadcopter model is shown in Fig. 2.3.

The fuselage dynamics and the quadcopter coordinate system are represented in Earth (**E**) and Body (**B**) frames. The **E** and **B** frames are used to describe relative motions of the quadcopter. To avoid nonlinearities in the quadcopter model, the following assumptions are made:

1. *The quadrotor's center of mass and frame origin are assumed to coincide*
2. *The quadrotor does not interact with the ground or any other surfaces*
3. *The quadrotor frame body is rigid and symmetrical*

A six (6) degree-of-freedom (DOF) model of the quadcopter can be derived using Lagrangian mechanics and the preceding assumptions. The model is valid in

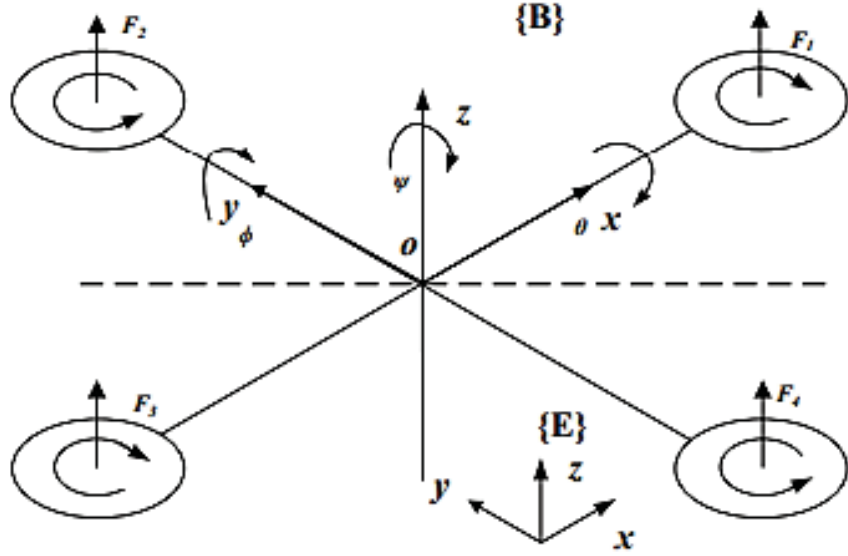


Figure 2.3: Free body diagram of a generic quadcopter, reprinted from Adaptive Controller Design for Generic Quadrotor Aircraft Platform Subject to Slung Load (IEEE 28th Canadian Conference on Electrical and Computer Engineering, 2015) [6].

hovering and low-speed flying modes. The resulting equations of motion are presented as follows:

$$\ddot{x} = \frac{U_1(\cos \phi \sin \theta \cos \psi + \sin \phi \sin \psi)}{M} \quad (2.2)$$

$$\ddot{y} = \frac{U_1(\sin \phi \sin \theta \cos \psi - \cos \phi \sin \psi)}{M} \quad (2.3)$$

$$\ddot{z} = \frac{U_1(\cos \phi \cos \psi)}{M} - g \quad (2.4)$$

$$\ddot{\phi} = \dot{\theta} \dot{\psi} \left( \frac{J_x - J_z}{J_x} \right) + \frac{l}{J_x} U_2 \quad (2.5)$$

$$\ddot{\theta} = \dot{\phi} \dot{\psi} \left( \frac{J_z - J_x}{J_y} \right) + \frac{l}{J_y} U_3 \quad (2.6)$$

$$\ddot{\psi} = \dot{\phi} \dot{\theta} \left( \frac{J_x - J_y}{J_z} \right) + \frac{l}{J_z} U_4 \quad (2.7)$$

where  $(x, y, z)$  are Cartesian coordinates;  $(\theta, \phi, \psi)$  are Euler angles corresponding to roll, pitch and yaw respectively;  $g$  is the acceleration due to gravity;  $M$  is the mass of the quadcopter;  $J_x, J_y, J_z$  are moments of inertia around the quadcopter's center of mass;  $l$  is the distance from the quadcopter's center of mass to its propellers; and the system inputs are  $U_1, U_2, U_3, U_4$ .

The system inputs can be obtained from the lift force of individual propellers as described below as follows:

$$U_1 = F_1 + F_2 + F_3 + F_4 \quad (2.8)$$

$$U_2 = F_3 - F_1 \quad (2.9)$$

$$U_3 = F_4 - F_2 \quad (2.10)$$

$$U_4 = F_1 + F_3 - F_4 - F_2 \quad (2.11)$$

Here  $U_1$  is the lifting thrust of the quadcopter or the lift input;  $U_2$  is the roll torque or roll input;  $U_3$  is the pitch torque or pitch input; and  $U_4$  is the yaw torque or yaw input. In Fig. 2.4, a pendulous load is attached to the generic quadcopter. The effects of the slung load on the model of a generic quadcopter are described below.

Assuming the quadcopter is suspended in the  $x$ - $z$  and  $y$ - $z$  planes, the distance between the quadcopter frame center of mass ( $o$ ) and the combined system center of mass ( $oo'$ ) is defined as  $c$  and  $L$  is the length of the pendulum cable. The offset ( $c$ ) can be ignored when  $L \gg c$ .

The position of the slung load in  $\mathbf{B}$  is defined as

$$\mathbf{r}^{\mathbf{B}} = \begin{bmatrix} 0 \\ 0 \\ L \end{bmatrix}. \quad (2.12)$$

While the position of the slung load in  $\mathbf{E}$  is defined as

$$\mathbf{r} = \mathbf{R} \begin{bmatrix} 0 \\ 0 \\ L \end{bmatrix}. \quad (2.13)$$

Where  $\mathbf{R} = \mathbf{Rot}(\alpha_y)\mathbf{Rot}(\alpha_x)$ .

The onset of oscillation in the slung load can induce significant instability in the quadcopter. As the mass of the slung load increases, the impact of pendulous behavior in the load becomes more severe. The mass of the UH FFP is minimal, and the automatic controllers found in commercial quadcopters are sufficient to compensate for any oscillations. Future designs of the FFP may result in increased mass and the need for a custom automatic controller may arise. In that event, the sliding mode controller described in [19] should be sufficient for stable operation of the quadcopter.

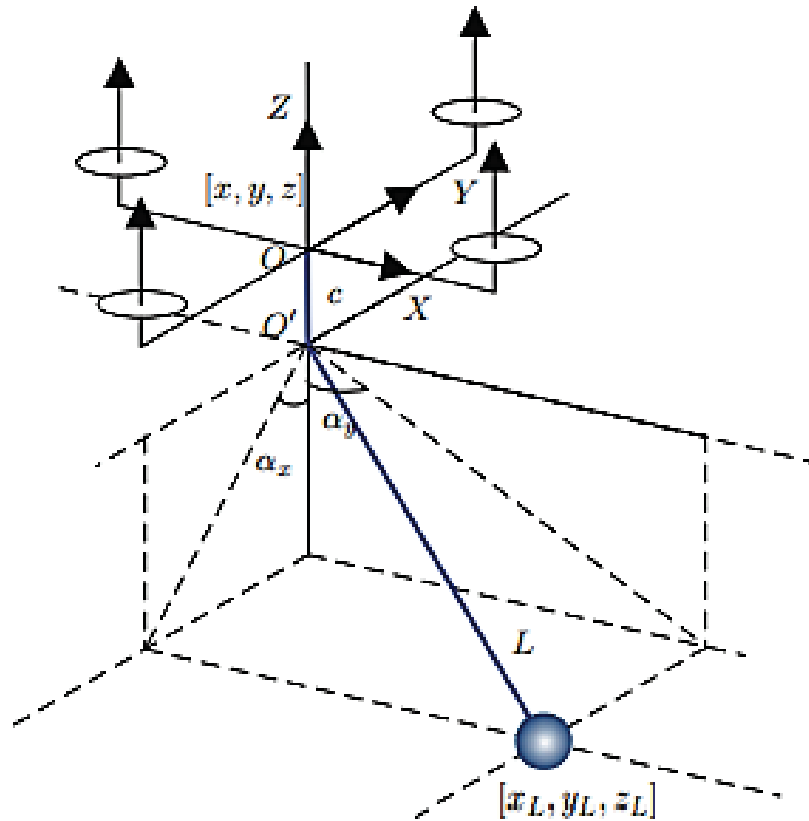


Figure 2.4: Generic quadcopter with an attached load, reprinted from Adaptive Controller Design for Generic Quadrotor Aircraft Platform Subject to Slung Load (IEEE 28th Canadian Conference on Electrical and Computer Engineering, 2015) [6].

## Chapter 3

### Methodology

This chapter describes the design, testing, and validation of the components used in the novel free-falling penetrometer (FFP) surveying method. The specifications of the UH FFP and its deployment vehicle are described in detail. The equipment and platforms used to validate the FFP are described. Detailed information is provided about the experimental procedure used in the validation process.

#### 3.1 Custom Free-Falling Penetrometer

The custom Free-Falling Penetrometer (FFP) designed by the University of Houston Robotic Swarm Control Lab (Figure 3.1) was optimized for aerial deployment.

The FFP was modeled after a miniature ballistic projectile with a  $25.4mm \times 340mm$  spike and a tail stabilizer. The FFP's payload is housed in a  $65mm \times 84mm$  volume. The FFP's electronic system comprises a 400g Sparkfun accelerometer (P/N H3LIS331DL) controlled by a Raspberry Pi Zero. The electronics system is powered by a series of Lithium-Potassium (Li-Po) batteries supplying 3.3V of electricity. The FFP's payload bay was toleranced to minimize unwanted vibrations in the  $x$  and  $z$  axes. For optimal stability, the payload was placed at the center of mass of the FFP. The accelerometer was oriented to align its  $y$ -axis with the FFP's  $y$ -axis. This

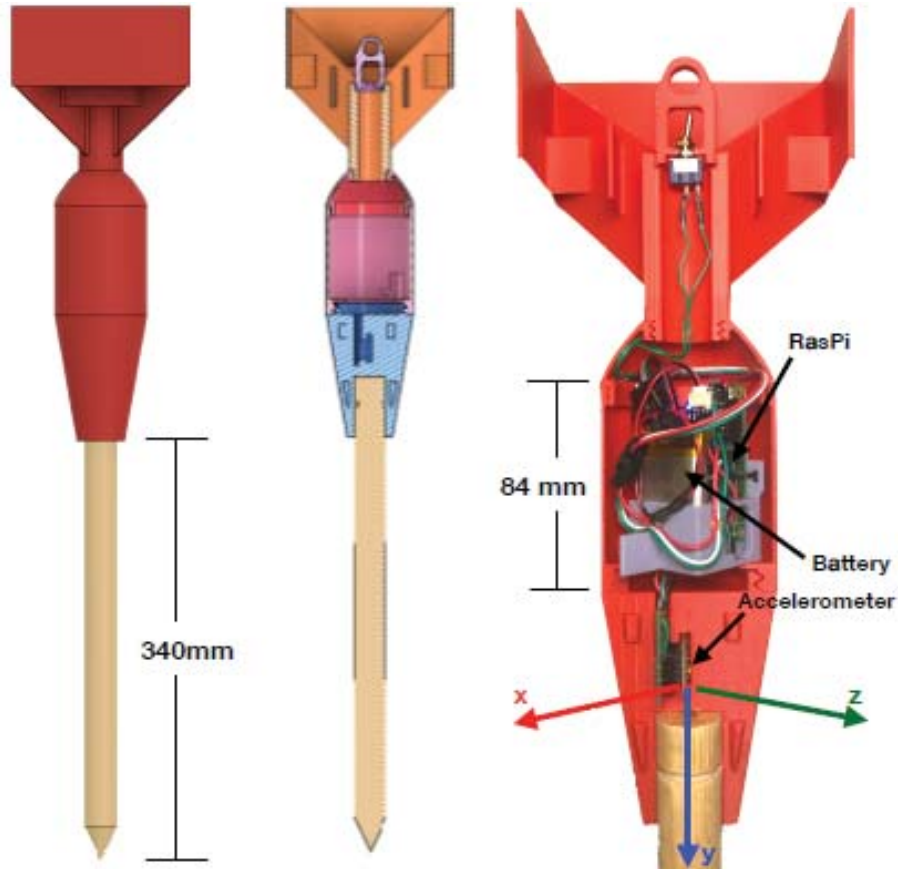


Figure 3.1: Custom FFP design with embedded electronics

orientation was selected to align the accelerometer with the direction of the FFP’s impact force upon deployment.

To minimize the weight on the deployment vehicle, the FFP was designed with lightweight components. The weight limitations of commercial quadcopters influenced selection of a wooden spike, lightweight Li-Po batteries, and low-infill 3D-printed components. By selecting these components, the UH FFP sacrificed mechanical robustness (but not accuracy) for the functionality of aerial deployment.

### 3.2 The Deployment Vehicle

A powerful commercial quadcopter was purchased to avoid the need to design an automatic controller for FFP deployment. Utilizing a commercial quadcopter

allows easy replication of the FFP surveying technique presented in this thesis. The experiments in Chapter 3 were performed using a Mavic Pro 2 drone. The Mavic was selected for its robust flight controller, intelligent situational awareness, and its autonomous waypoint navigation feature. The Mavic has a gross take-off weight (GTOW) of 907g, a maximum flight speed of 72kph and a maximum ascent speed of 5m/s [1]. The UAV (shown in Fig 3.2) was operated using its attached remote controller. The Mavic's GTOW imposed limitations on the payload and the extraction techniques described later in this thesis.



Figure 3.2: FFP deployment vehicle, shown in loaded and unloaded configurations

### 3.3 Description of Soils

The proposed surveying technique was tested in three soil samples. The soil samples are representative of the range of soils typically found in the wetlands. The first was *torpedo sand*. Torpedo sand is a naturally occurring, coarse-grained sand and gravel mix. The second soil was *beach volleyball sand*. Standard beach volleyball sand consists of at least 80% 0.5mm - 1.0mm particles. The third soil was *saturated marsh mud*. These samples were obtained from a local supplier of soil and are shown in Fig. 3.3.

The water content of each soil was estimated by measuring the change in mass after a volume of soil was dried 100°C for 48 hours in a lab furnace. The water content of the torpedo sand was 7.46%, the volleyball sand was 11.68%, and the saturated mud was 30.5%.



Figure 3.3: Representative specimen of wetlands soil used in this experiment.

## 3.4 Test Beds

Components of the proposed wetlands surveying technique were tested using five (5) distinct test-beds. This section describes the design of these test-beds.

### 3.4.1 Drop Test Bed

The functionality of the UH FFP was validated in a series of drop tests. The FFP was dropped into 25 gallon containers filled with the three soil samples described in the previous section. The drops were performed using a pulley system to ensure consistency between drops. The soil in the containers were prepared between tests to simulate virgin soil. Drop heights were measured as the distance from the tip of the spike to the top of the soil as shown in Fig. 3.4

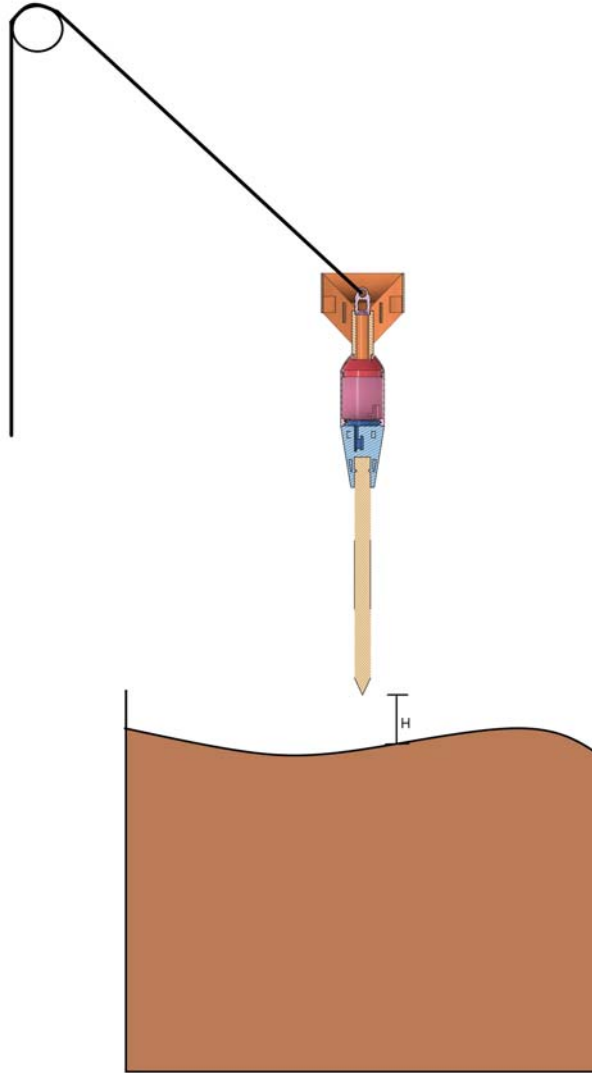


Figure 3.4: Drop test-bed with pulley.

### 3.4.2 Linear Actuator Extraction Test Bed

The force dynamics during the extraction of a free-falling penetrometer (FFP) is the determining factor for a successful UAV deployment and retrieval. A one-meter-long linear actuator (OpenBuildsPartStore.com, C-Beam) was used to generate the force needed to overcome the mud suction force experienced by a deployed FFP. A 1.5mm steel cable connects the linear actuator and the FFP. An S-Type load cell (10kg, CALT) is inserted between the FFP and the linear actuator. A schematic of

the test-bed is shown in Fig 3.5.

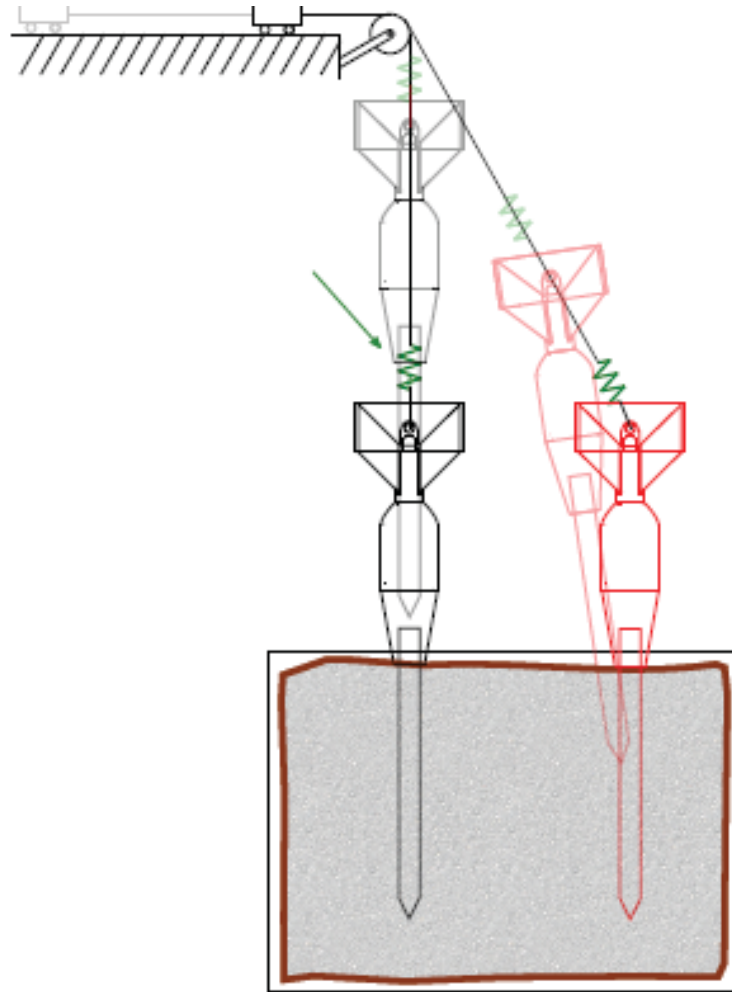


Figure 3.5: Schematic of the linear actuator test-bed showing vertical and angled tests.

After fully inserting the FFP spike into a mud sample, the linear actuator pulls the FFP until the tip of the FFP is at least  $3mm$  from the surface of the mud sample. The tension in the steel cable is measured by the load cell. Multiple tests were performed to determine the effect of speed and angle on the extraction force.

### 3.4.3 Drone Dynamics and Stability Test Bed

A series of tests were devised to characterize the quadcopter's dynamics and stability characteristics. Of particular interest was its maximum stable lifting force,

jerk force and tethered pulling angle. The test-bed in Fig. 3.6 was designed to aid in the characterization of these properties.

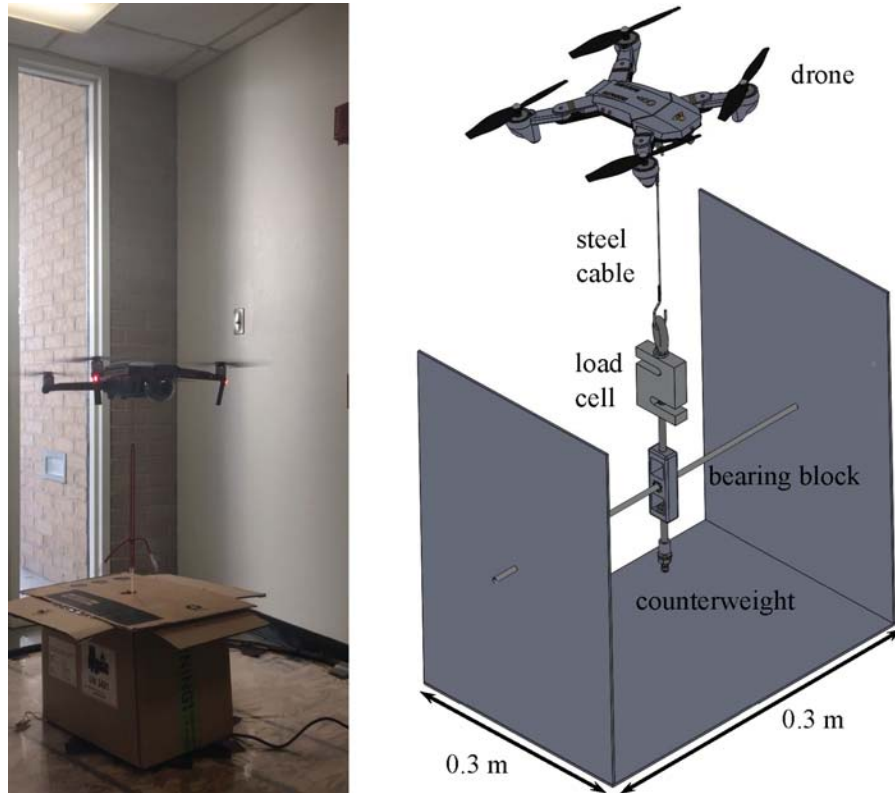


Figure 3.6: The drone dynamics and stability test platform early model (left) and final model (right).

The final test-bed comprises a  $0.3m \times 0.3m \times 0.3m$  scaffolding frame, an S-type load cell ( $5kg$ , CALT), a bearing block, and a counterweight. The bearing block/counterweight/load cell assembly (shown in Fig 3.7) was designed to minimize rotational inertia around the central axle.

By minimizing rotational inertia around the central axle, the test-bed is able to accurately capture the lateral lifting force of the quadcopter. As seen in Fig 3.7, the sides of the final test-bed are marked to allow easy estimation of the lateral tethered pulling angle. The quadcopter is connected to the test-bed via a  $1.5mm$  steel cable. The load cell records any applied forces.

The lateral stability properties of the quadcopter are determined by measuring



Figure 3.7: Detailed view of the bearing block/counterweight/load cell assembly.

the lifting properties of the quadcopter at different angles. Upon reaching the extent of its tether to the test-bed, the quadcopter attempts to maintain lift while undergoing lateral translation. The orientation of the load-cell/counterweight system changes to match the angle of the tethering steel cable. The load cell records the transient and steady-state forces generated by the lateral translation.

The quadcopter's maximum stable lifting and jerk forces are determined by measuring the lifting force of the drone at  $90^\circ$ . After a rapid takeoff, the load cell records the transient jerk forces generated by the quadcopter upon reaching the limit of its tether. After reaching the limit of its tether, the quadcopter maintains the maximum lifting speed for 20 to 30 seconds. The load cell records the steady-state lifting force generated by the quadcopter maintaining its maximum lifting speed. The process is repeated at various angles to characterize the effects of tether angle on the maximum stable lifting and jerk force.

### 3.4.4 Quadcopter Deployment Test Bed

The novel surveying technique was validated through a series of live tests. The tests were conducted indoors in an industrial warehouse. The quadcopter deployment test environment is shown in Fig. 3.8.

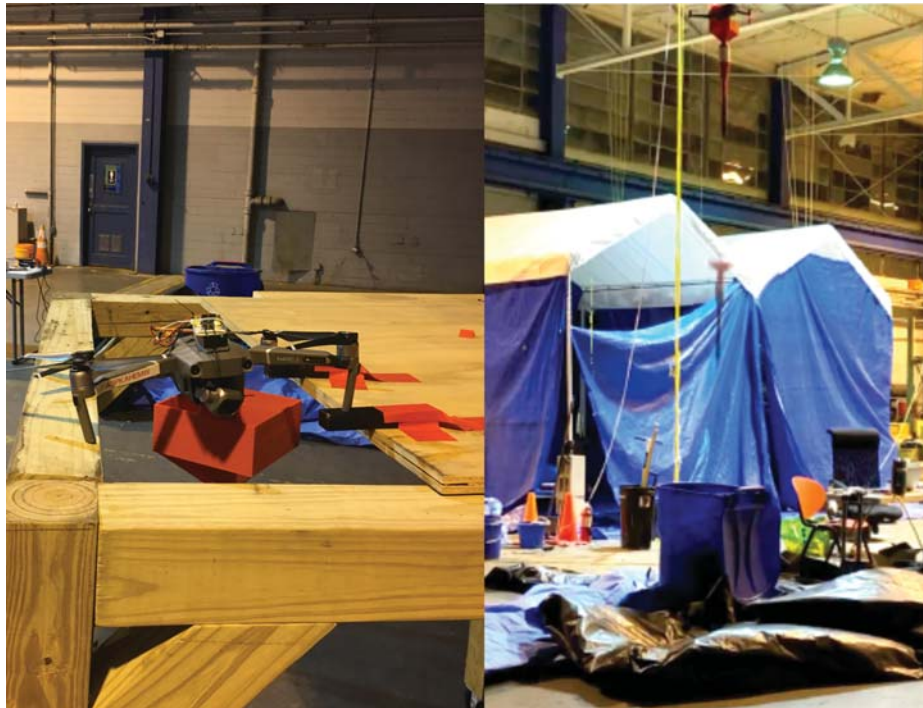


Figure 3.8: FFP deployment using a UAV.

The quadcopter was under manual control for the duration of the deployment tests. In addition to its payload (the FFP), the quadcopter was equipped with a remote controlled (RC) receiver and a release servo. Upon the receiving an activation signal, a section of the release servo is unlatched from the quadcopter frame. The activation signal is sent through the RC receiver.

All components used in the deployment tests are securely attached before take-off. After takeoff, the drone is manually piloted to a specified height and drop point. The drone hovers over a 25 liter bin filled with a representative sample of wetlands mud. After verifying the drop location, an activation signal is sent to the release

servo and the FFP is released into the mud sample bin. Impact data from the drop is recorded in the Raspberry Pi Zero housed in the FFP.

After a successful drop, the quadcopter hovers at a safe height and a  $1.5mm$  steel cable is used to tether it to the FFP. The tethered quadcopter ascends and the FFP is extracted in the process. It is important to note that some quadcopters may not be able to overcome the mud suction force holding the FFP. A slight modification was made to the FFP to accommodate weaker quadcopters. Introducing a sacrificial sleeve reduces the lifting force required to extract the FFP. A sacrificial sleeve based on the design in Fig. 3.9 was used for some of the experiments in this thesis.

Before extraction attempts begin, an S-Type load cell ( $10kg$ , CALT) is inserted in the line between the FFP and the quadcopter. The load cell records the force-time history of each extraction attempt. An example of a successful extraction attempt is shown in Fig. 3.10. After a successful extraction, the quadcopter hovers at a safe height and the payload is disconnected.

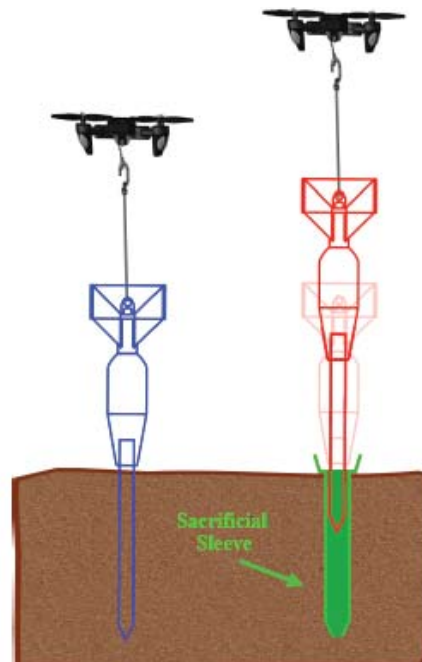


Figure 3.9: Schematics of sacrificial sleeve tests



Figure 3.10: Successful extraction of FFP

### 3.4.5 Reel Mechanism Test Bed

Completion of the quadcopter deployment test led to the recognition of the limitations of the RC release servo mechanism. The amount of manual intervention required for a successful deployment test made it an unfeasible solution. The reel mechanism was built to capitalize on the strengths on the RC release servo mechanism while avoiding its limitations. The reel mechanism (shown in Fig. 3.11) comprises a Zebco fishing reel (202ZK), a HiTec servomotor (HS-805BB), and a Pololu 131:1 DC motor (P/N:2827). The mechanism allows for remote or automated deployment and retrieval. The FFP is released by sending an activation signal to the servomotor. The motor actuates the reel release and the FFP is deployed. After overcoming the mud suction force holding the FFP (manually or with a sacrificial sleeve), the DC motor reels in the FFP and the system can move to a different location for a new test.



Figure 3.11: Reel mechanism (incomplete)

## Chapter 4

### Results

This chapter presents the data obtained from experiments on the test-beds described in the previous section. Acceleration-time histories and penetration depths are used to classify wetland soil types. The transient and steady state forces needed to extract a deployed free-falling penetrometer (FFP) are discussed. Finally, the force profile of a successful FFP retrieval is explained

#### 4.1 Drop Tests

The drop tests validate the FFP by considering the effects of drop altitudes on FFP acceleration-time histories. The acceleration-time history data may be used to distinguish soil types. The drop heights tested were  $1.5m$ ,  $2.5m$ , and  $3.7m$ . The results are seen in Fig. 4.2, Fig. 4.2, and Fig. 4.3 below.

Successive drop tests at the specified heights result in the trends seen in the acceleration-time history plots in Fig. 4.2, Fig. 4.2, and Fig. 4.3. The acceleration starts at zero as the FFP is dropped from the specified height. The peak deceleration occurs as the FFP contacts the surface of the soil. The deceleration rate goes to zero as the FFP penetrates the soil and comes to a rest.

The effect of drop height on peak deceleration is easily observable. For each soil type, there is a semi-linear relationship between the peak decelerations in Fig 4.1

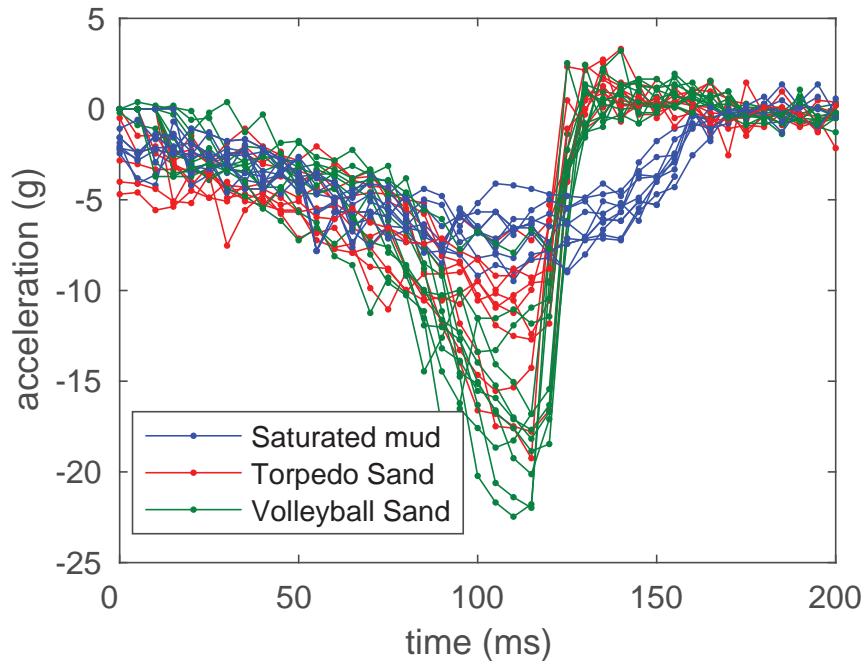


Figure 4.1: Measuring the effect of a 1.5m drop on FFP acceleration-time history

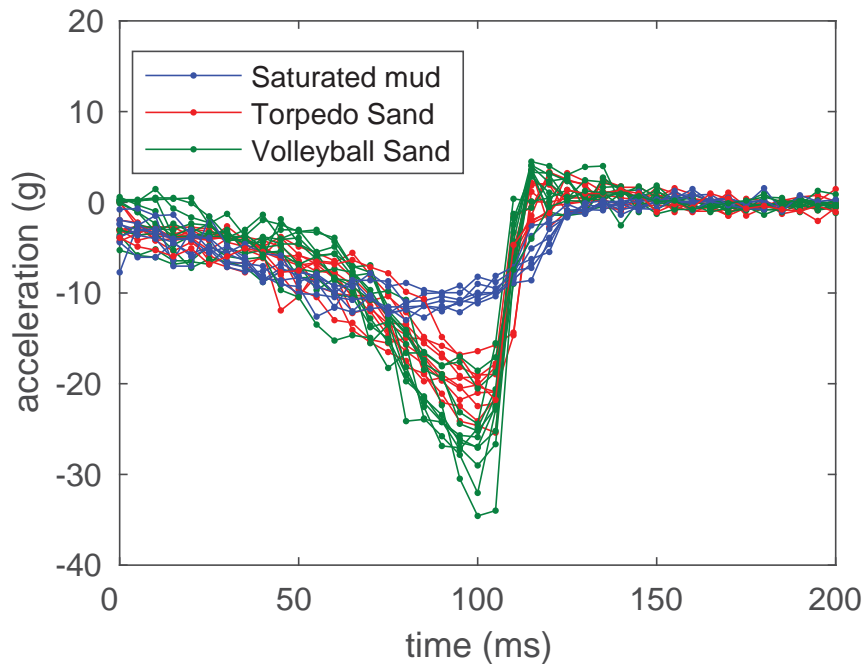


Figure 4.2: Height: 2.5 m

and 4.3. While individual soil types are recognizable at 1.5m, there is significant overlap between all soil types. At 3.7m, it becomes easier to distinguish mud from

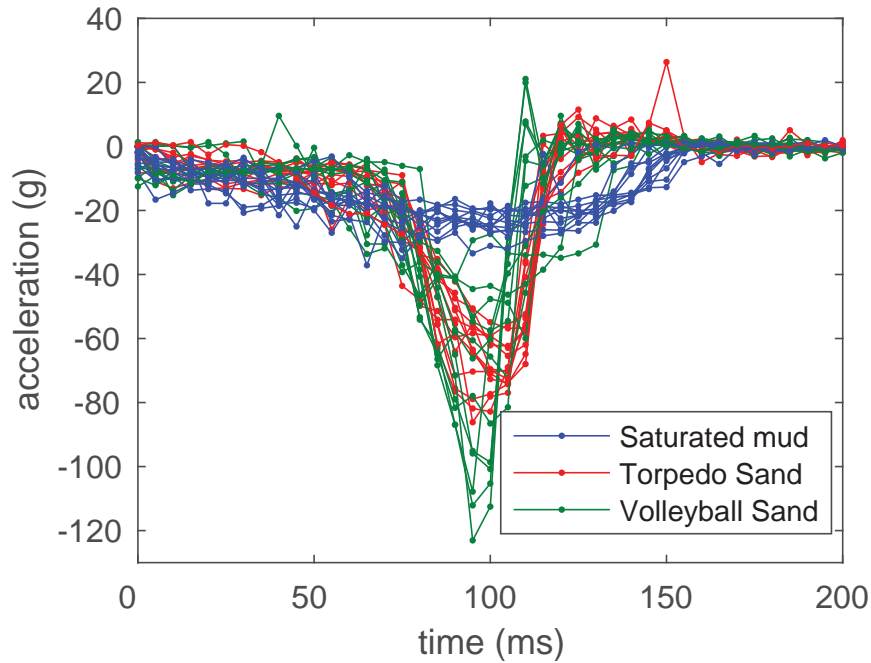


Figure 4.3: Height: 3.7 m

sand but there is significant overlap between sand types. The peak deceleration of sand is much higher than the peak deceleration of mud. From this information, it can be deduced that sand is stiffer than clay. It is also presumed that torpedo sand and volleyball sand have similar stiffness coefficients. Visual inspection of the plots indicate reproducibility in the data.

Another interesting trend observed in the acceleration-time histories shown in Figures 4.1 to 4.3, are the differences in the area under the curve for each soil. The narrower area under the curve for sands indicates that the FFP settles quicker in sand than in mud. This suggests the FFP penetrates less in sand than in mud. This assumption is confirmed in Fig 4.4 as the average penetration depth in mud is  $100mm$  greater than the penetration depth in sand. This suggests a minimum drop height of  $3m$  is needed for successful penetration.

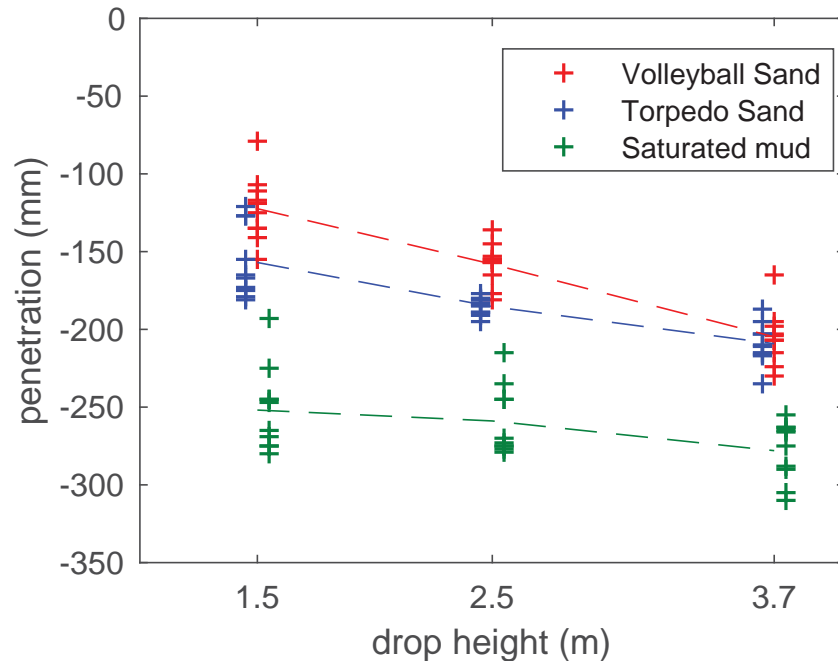


Figure 4.4: Penetration Depth as a function of drop height and soil type.

## 4.2 Actuator Extraction Tests

As described in the methodology, a linear actuator was used to extract a FFP buried in mud. The relationship between extraction speed, extraction angle, and extraction force was considered. Angle variation was achieved by changing the position of the mud bin relative to the fixed linear actuator. Three (3) extraction angles were selected to determine the relationship between extraction angle and extraction force. The selected extraction speeds were  $70^\circ$ ,  $80^\circ$ , and  $90^\circ$ . The results are shown in Fig. 4.5.

Three (3) extraction speeds were selected to determine the relationship between extraction speed and extraction force. The selected extraction speeds were  $13.6\text{mm/s}$ ,  $27.3\text{mm/s}$ , and  $333\text{mm/s}$ . To achieve a speed of  $333\text{mm/s}$ , the stepper motor in the linear actuator was replaced with a drill motor. The results are shown in Fig. 4.6.

The effect of angle on the FFP extraction force at a speed of  $27.3\text{mm/s}$  is shown

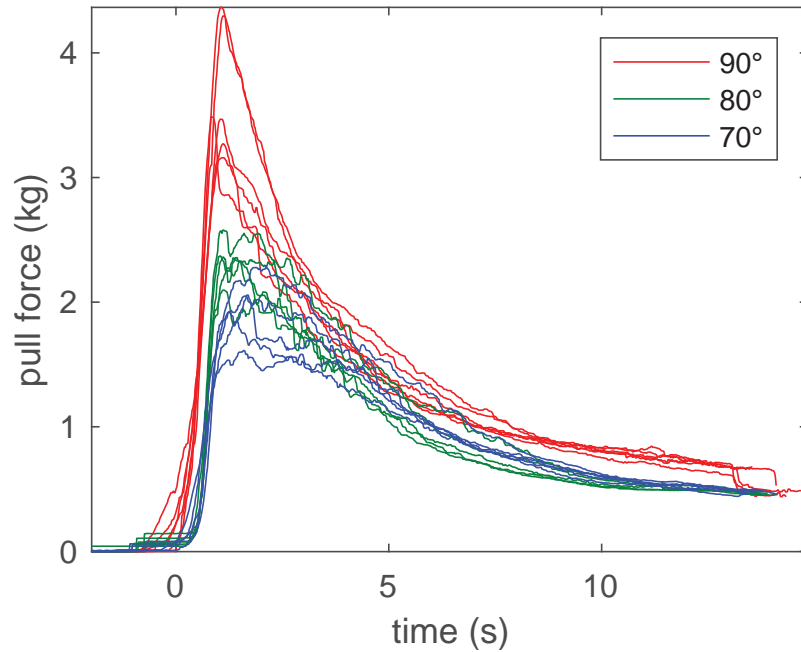


Figure 4.5: Relationship between extraction force and extraction angle

in Fig. 4.5. The trend suggests that the extraction force is reduced as the extraction angle deviates from the vertical axis. The extraction force at  $90^\circ$  is 1.75 times higher than the extraction force at  $70^\circ$ . This trend might be caused by the introduction of a moment as the extraction angle varies from  $90^\circ$ . The rotation caused by the moment loosens the mud and reduces the suction force.

The effect of speed on the extraction force at  $90^\circ$  is shown in Fig. 4.6. The extraction force increases with the extraction speed. This increase may be attributed to the viscoelastic behavior of mud. The wetlands mud sample might be a dilatant, a material whose viscosity increases as the shear rate increases.

### 4.3 Quadcopter Dynamics and Stability Tests

The maximum lifting force of the Mavic Pro 2 quadcopter was measured on the dynamics and stability test-bed as described in the methodology. The transient and

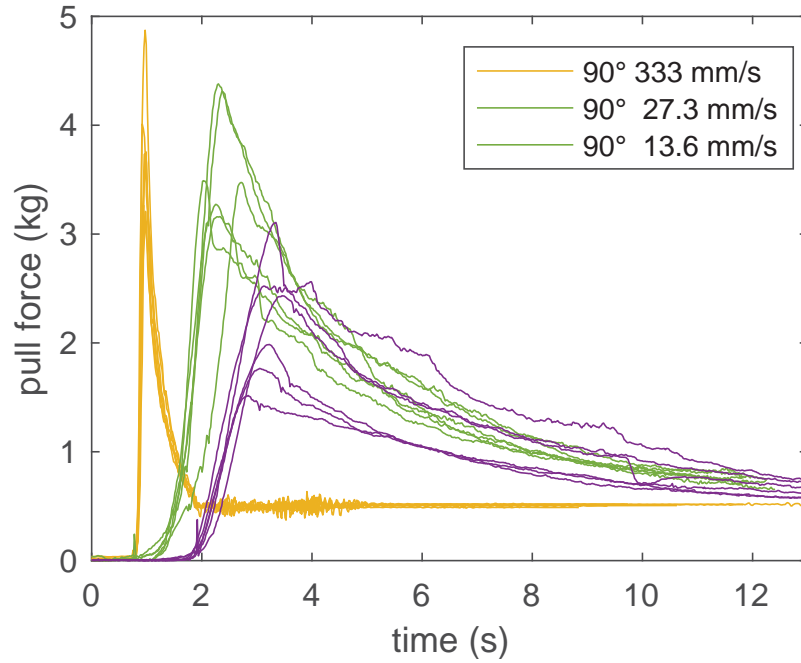


Figure 4.6: Relationship between extraction force and extraction speed

steady state forces generated while attempting to liftoff at maximum speed are shown in Fig. 4.7.

Multiple tests confirmed that the steady-state lifting force of the Mavic at  $90^\circ$  is  $970g$ . Upon reaching the extent of its tether, the quadcopter generated transient forces of more than  $3kg$ . This oscillations caused by this jerk were quickly eliminated and the quadcopter remained stable. This behavior confirms that the Mavic’s intelligent flight controller is sufficient FFP surveying expeditions. It is important to note that the peak forces generated by the quadcopter are less than the peak forces generated while extracting the FFP.

While conducting linear actuator extraction tests, the relationship between extraction force and angle was noted. The angular lifting force of the Mavic was measured on the dynamic and stability test-bed. The results are shown in Fig. 4.8.

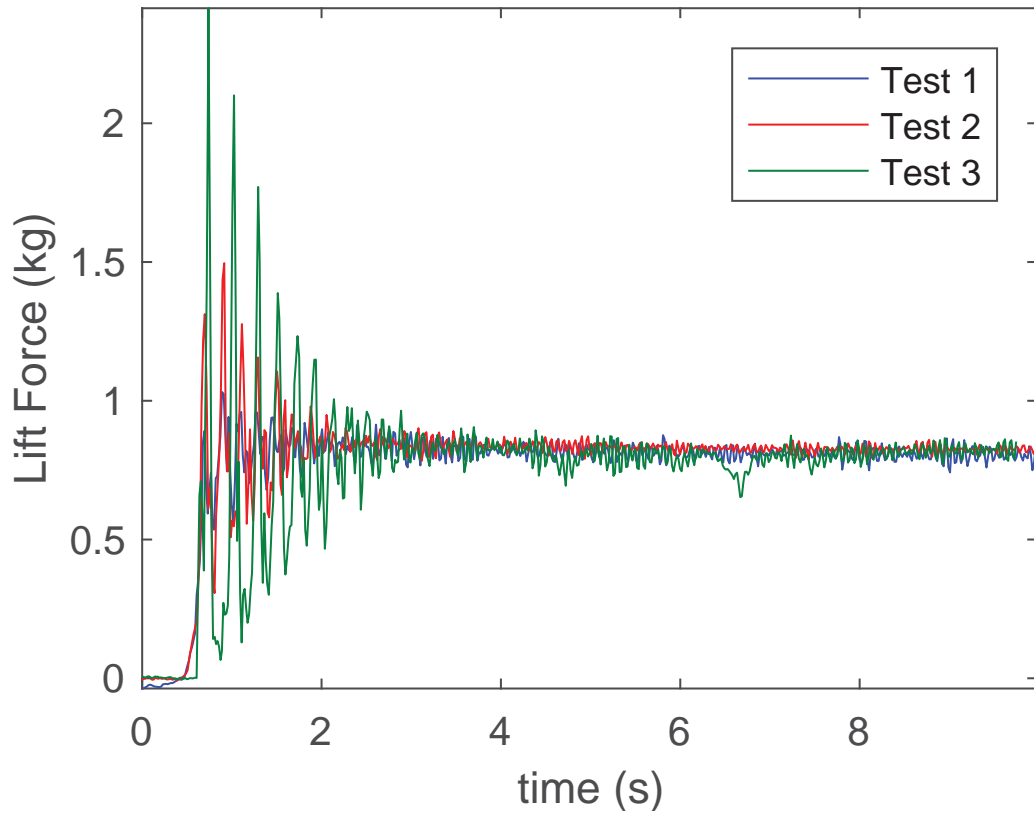


Figure 4.7: Maximum drone lift at 90°

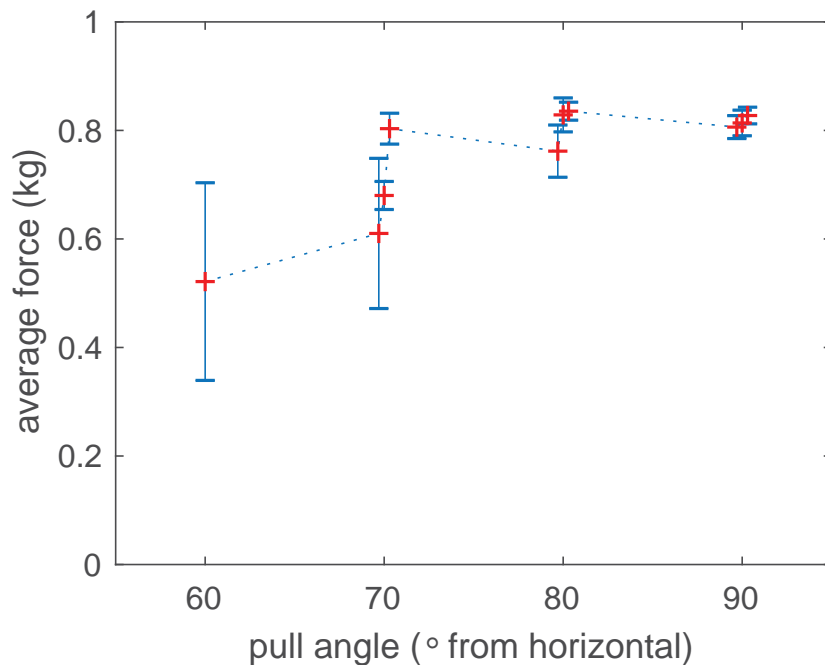


Figure 4.8: Angular drone lifting forces

While the quadcopter maintained its maximum lifting force within a  $10^\circ$  band, larger variations from the vertical axis induced instability. The quadcopter barely remained airborne at  $60^\circ$ . The destabilizing effect of the tether at steep angles is poorly understood. It is important to note that angular peak force is less than the peak force needed to extract the FFP at an angle. This suggests that the lifting power of the Mavic Pro 2 is insufficient for FFP extraction.

## 4.4 Deployment Tests

Multiple FFPs were used to conduct the deployment tests. The quadcopter was manually piloted to a specified GPS coordinate and the FFPs were dropped from a height of  $3.7m$  ( $12ft$ ). Aerial drop tests were hindered by the limitations of the deployment test-bed. The  $25L$  bin proved to be a difficult target for the FFP and slight variations in the quadcopter's orientation resulted in damage to the FFP as the stabilizer struck the edge of the bin.

After each successful drop, a load cell and a  $1.5mm$  diameter steel cable is inserted between the FFP and the quadcopter. After the quadcopter is tethered to the FFP, it attempts an ascent at the maximum speed and its lifting force is transmitted to the FFP stuck in the mud. The generated force is recorded by the load cell and the results are shown in Fig. 4.9.

The Mavic Pro 2 quadcopter was unable to extract the FFP without external assistance. The oscillations observed in the blue curve shown in Fig 4.9 are a result of lateral tugs applied to the FFP. Despite changing the extraction angle, the quadcopter was unable to complete an unaided extraction of the FFP. This is explained by the results of Fig. 4.8 which shows the relationship between angle and the quadcopter's lifting force. The results from Fig. 4.8 show that the forces at  $60^\circ$  is  $0.52 \pm 0.18$  kg, at  $70^\circ$  is  $0.70 \pm 0.06$  kg, at  $80^\circ$  is  $0.81 \pm 0.03$  kg, and at  $90^\circ$  is  $0.82 \pm 0.02$  kg. While

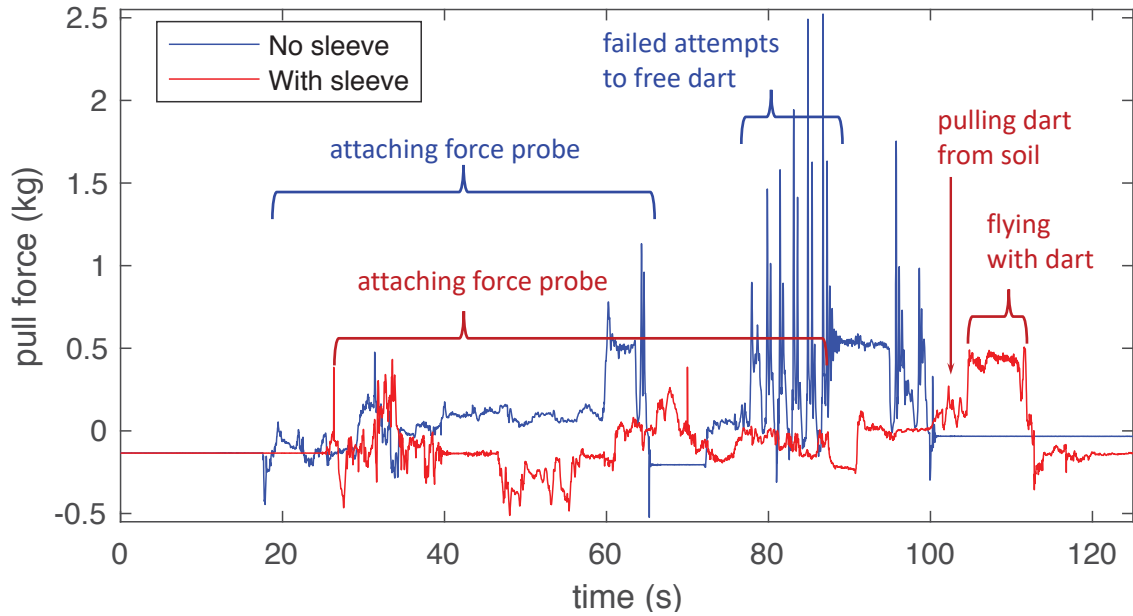


Figure 4.9: FFP extraction attempts, blue: extraction without a sacrificial sleeve, red: extraction with a sacrificial sleeve

these values are comparable to the steady state extraction forces shown in Fig. 4.5, they are less than the transient peak forces required to extract the FFP.

Note that this is a limitation of the selected quadcopter (Mavic Pro 2). The transient and steady state extraction forces shown in Fig. 4.8 are within the specifications of many commercial quadcopters.

The deployment tests were repeated using an FFP with a sacrificial sleeve as described in Fig. 3.9. The sleeve was designed to fit loosely around the FFP spike. A thin foam gasket was inserted between the sleeve and the FFP to dampen impact vibrations. The sacrificial sleeve significantly reduced the force needed to extract the FFP as observed in Fig. 4.9. The introduction of the sacrificial sleeve reduced the extraction force sufficiently for the Mavic quadcopter to retrieve the FFP. Note that the peak extraction force of the successful sleeve deployment test (red) in Fig 4.9 is comparable to the steady state extraction force in Fig 4.5.

#### 4.4.1 Reel Mechanism Tests

Limitations of the servo release mechanism described in the methodology are addressed by the reel mechanism. After overcoming the mud suction force holding the FFP, the reel mechanism retracts the FFP and allows for multiple unaided deployment tests. The release and retraction subsystems have been validated on the reel mechanism prototype, and the assembled mechanism awaits a complete deployment test.

## Chapter 5

### Conclusion

Advances in robotics and UAV technology can enable environmental scientists to explore new testing techniques. By taking advantage of the ubiquity of commercial quadcopters, scientists can improve existing methods of quantifying how coastal ecosystems change with under the effects of sea-level rise and global climate change. As environmental stressors caused by climate change worsen, there arises a need for more frequent field measurements taken over larger spatial regions.

This thesis presented a novel method for conducting free-falling penetrometer (FFP) tests in the wetlands using a custom-designed, aerial deployable penetrometer. The method represents a significant cost improvement over conventional core collection and cone penetrometer tests (CPTs). The method was designed using cheap, commercially-available components and the experiments are easily replicated in the field.

The method was validated by quantifying the deceleration profile, penetration depth, and extraction force of the FFP at various heights. The method was used to identify representative samples of wetlands sand and mud. Information about soil strength and viscosity can be deduced from the FFP deceleration profile and penetration depth. Extraction force tests were used to characterize the mud suction force experienced by the FFP. Investigations into the relationship between extraction

force, extraction speed, and extraction angle revealed that a slow, angled pulling force is required to minimize the mud suction force. The information obtained from the extraction force tests should inform the selection of a commercial quadcopter for field experiments. Limitations on the lifting specifications of the quadcopter can be overcome by inserting a loosely-fit, sacrificial sleeve onto the FFP.

The experiments in this study proved the feasibility of aurally deployed free falling penetrometers (FFPs). The method can be used to obtain insights into wetlands soil properties while minimizing experimentation costs.

## **5.1 Future Work**

While the reel mechanism addresses the some of the limitations of the method presented in this study, more data is needed to validate its reliability. Further improvements should be made to the sacrificial sleeve. It could be made from bio-degradable materials to reduce the ecological damage to the wetlands. There is ongoing research at the University of Houston Robotic Swarm Control Lab to automatically classify soft soils using deceleration profile data and machine learning.

## References

- [1] “Mavic 2 - specifications, faqs, videos, tutorials, manuals - dji.” [Online]. Available: <https://www.dji.com/mavic-2/info#specs>
- [2] *Standard operating procedure for collection of sediment samples: GSL impounded wetland 2012 monitoring activities*. State of Utah Department of Environmental Quality, Department of Water Quality, 2011.
- [3] V. M. Baez, A. Shah, S. Akinwande, N. H. Jafari, and A. T. Becker, “Assessment of soil strength using a robotically deployed and retrieved penetrometer,” in *under review*. tbd, 2020, p. tbd.
- [4] S. Collico, N. Perez, M. Devincenzi, and M. Arroyo, “Applying bayesian updating to cpt data analysis,” in *Cone Penetration Testing 2018: Proceedings of the 4th International Symposium on Cone Penetration Testing (CPT’18), 21-22 June, 2018, Delft, The Netherlands*. CRC Press, 2018, p. 221.
- [5] T. E. Dahl, *Status and trends of wetlands in the conterminous United States 2004 to 2009*. US Department of the Interior, US Fish and Wildlife Service, Fisheries and Habitat Conservation, 2011.
- [6] Y. Feng, C. A. Rabbath, S. Rakheja, and C.-Y. Su, “Adaptive controller design for generic quadrotor aircraft platform subject to slung load,” in *2015 IEEE 28th Canadian Conference on Electrical and Computer Engineering (CCECE)*. IEEE, 2015, pp. 1135–1139.

- [7] J. T. Morris, D. C. Barber, J. C. Callaway, R. Chambers, S. C. Hagen, C. S. Hopkinson, B. J. Johnson, P. Megonigal, S. C. Neubauer, T. Troxler *et al.*, “Contributions of organic and inorganic matter to sediment volume and accretion in tidal wetlands at steady state,” *Earth’s future*, vol. 4, no. 4, pp. 110–121, 2016.
- [8] G. K. Mulukutla, L. C. Huff, J. S. Melton, K. C. Baldwin, and L. A. Mayer, “Sediment identification using free fall penetrometer acceleration-time histories,” *Marine Geophysical Research*, vol. 32, no. 3, pp. 397–411, 2011.
- [9] M. Mumtaz, N. Stark, and S. Brizzolara, “Pore pressure measurements using a portable free fall penetrometer,” in *Cone Penetration Testing 2018: Proceedings of the 4th International Symposium on Cone Penetration Testing (CPT’18), 21-22 June, 2018, Delft, The Netherlands*. CRC Press, 2018, p. 461.
- [10] M. B. Mumtaz, “Investigation of pore pressures during high-velocity impact by a free fall penetrometer,” Ph.D. dissertation, Virginia Tech, 2018.
- [11] M. Nazem, J. P. Carter, D. W. Airey, and S. Chow, “Dynamic analysis of a smooth penetrometer free-falling into uniform clay,” *Géotechnique*, vol. 62, no. 10, pp. 893–905, 2012.
- [12] A. Plowcha, Y. Sun, C. Detweiler, and J. Bradley, “Predicting digging success for unmanned aircraft system sensor emplacement,” in *International Symposium on Experimental Robotics*. Springer, 2018, pp. 153–164.
- [13] D. Scavia, J. C. Field, D. F. Boesch, R. W. Buddemeier, V. Burkett, D. R. Cayan, M. Fogarty, M. A. Harwell, R. W. Howarth, C. Mason *et al.*, “Climate change impacts on us coastal and marine ecosystems,” *Estuaries*, vol. 25, no. 2, pp. 149–164, 2002.
- [14] T. Shaw, J. Clear, B. Horton, N. Khan, D. Nikitina, M. D. Enache, M. Potapova, D. Frizzera, N. Procopio, C. H. Vane *et al.*, *New Jersey (USA) wetlands past*,

*present and future: using sediment archives to inform and guide wetland protection, restoration and resilience.* New Jersey Department of Environmental Protection, 2016.

- [15] N. Stark, B. Radosavljevic, B. Quinn, and H. Lantuit, “Application of portable free-fall penetrometer for geotechnical investigation of arctic nearshore zone,” *Canadian Geotechnical Journal*, vol. 54, no. 1, pp. 31–46, 2017.
- [16] R. Stewart, L. Chang, S. Sudarshan, A. Becker, and L. Huang, “An unmanned aerial vehicle with vibration sensing ability (seismic drone),” in *SEG Technical Program Expanded Abstracts 2016*. Society of Exploration Geophysicists, 2016, pp. 225–229.
- [17] S. K. Sudarshan, L. Huang, C. Li, R. Stewart, and A. T. Becker, “Seismic surveying with drone-mounted geophones,” in *2016 IEEE International Conference on Automation Science and Engineering (CASE)*. IEEE, 2016, pp. 1354–1359.
- [18] S. K. Sudarshan, V. Montano, A. Nguyen, M. McClimans, L. Chang, R. R. Stewart, and A. T. Becker, “A heterogeneous robotics team for large-scale seismic sensing,” *IEEE Robotics and Automation Letters*, vol. 2, no. 3, pp. 1328–1335, 2017.
- [19] B. Sumantri, N. Uchiyama, S. Sano, and Y. Kawabata, “Robust tracking control of a quad-rotor helicopter utilizing sliding mode control with a nonlinear sliding surface,” *Journal of System Design and Dynamics*, vol. 7, no. 2, pp. 226–241, 2013.
- [20] Y. Sun, A. Plowcha, M. Nail, S. Elbaum, B. Terry, and C. Detweiler, “Unmanned aerial auger for underground sensor installation,” in *2018 IEEE/RSJ International Conference on Intelligent Robots and Systems (IROS)*. IEEE, 2018, pp. 1374–1381.

- [21] D. White, C. O’Loughlin, N. Stark, and S. H. Chow, “Free fall penetrometer tests in sand: Determining the equivalent static resistance,” in *Cone penetration testing 2018: Proceedings of the 4th international symposium on cone penetration testing*. CRC Press Boca Raton, FL, USA, 2018, pp. 695–701.

